Word Count: 6550 (Revision 2)

Thermal conductivity of single-crystal brucite at high pressures with implications for thermal anomaly in the shallow lower mantle

Yu-Hsiang Chien[1,2,3*], Kai-Chi Wei[4], and Wen-Pin Hsieh[2,4*]

[1]Earth System Science Program, Taiwan International Graduate Program (TIGP), Academia Sinica and National Central University, Taipei 11529, Taiwan

[2]Institute of Earth Sciences, Academia Sinica, Nankang, Taipei 11529, Taiwan

[3]College of Earth Sciences, National Central University, Taoyuan 32001, Taiwan

[4]Department of Geosciences, National Taiwan University, Taipei 10617, Taiwan

Corresponding authors: Yu-Hsiang Chien (yhchien@gate.sinica.edu.tw) and Wen-Pin Hsieh (wphsieh@earth.sinica.edu.tw)

Abstract

Brucite ($Mg(OH)_2$) is an important hydrous mineral in the MgO-SiO_2-H_2O system and also a key component in the process of hydrothermal metamorphism. Due to its large water storage capacity and presence within a sinking slab, study of brucite's physical

properties under relevant extreme conditions could shed new lights on its potential impacts on slab's thermal profile and geodynamics, as well as seismic anomaly observed around a subduction zone. For example, seismic tomography has revealed slab stagnation and low-velocity zones in the shallow lower mantle that are conventionally attributed, respectively, to large contrasts of physical properties between the slab and mantle as well as dehydration melt. However, the effect of hydrous minerals on slab dynamics and seismic anomalies remains poorly understood. Here we study thermal conductivity of brucite at high pressures and room temperature as well as at ambient pressure and elevated temperatures. We further model thermal conductivity of brucite along a representative geotherm and find an ~6–19-fold increase in the thermal conductivity as brucite decomposes to periclase in the shallow lower mantle (~800 km depth). This result implies that the subduction and decomposition of brucite-rich aggregate within a slab may create a local high-temperature anomaly that would both enhance the slab's buoyancy, leading to stagnation, and facilitate dehydration melting, contributing to seismic low-velocity zones. Our findings offer mechanisms associated with brucite decomposition that could influence the slab dynamics and seismic structures in the shallow lower mantle.

Keywords: brucite, hydrous mineral, anisotropic thermal conductivity, slab stagnation, dehydration melting

Introduction

Brucite is one of the key hydrous phases in the complex MgO-SiO_2-H_2O (MSH) ternary system (Hacker et al., 2003; Ohtani et al., 2000; Ohtani et al., 1995). It contains large amounts of water (~30 wt%) and can coexist with other hydrous minerals, e.g., phase D, at pressure-temperature (*P-T)* conditions within a subducting slab at mantle transition zone and top of lower mantle (Irifune et al., 1998; Nishi et al., 2014; Ohtani et al., 2000; Ohtani et al., 1995). Presence of brucite in Earth's deep interior could play a crucial role in affecting Earth's deep water circulation and water budget. In the past decades, many physical properties of brucite under extreme conditions have been extensively investigated, including 1) phase stability (Fukui et al., 2005; Hacker et al., 2003; Hermann and Mookherjee, 2016; Nishi et al., 2014; Pawley and Wood, 1996), 2) elastic properties and seismic velocities (Hermann and Mookherjee, 2016; Jiang et al., 2006; Mainprice and Ildefonse, 2009), 3) atomic structure and equation of state (Catti et al., 1995; Hermann and Mookherjee, 2016; Mookherjee and Stixrude, 2006; Nagai et al., 2000; Parise et al., 1994; Raugei et al., 1999; Xia et al., 1998), 4) molecular vibrational

spectrum (Duffy et al., 1995; Kruger et al., 1989; Zhu et al., 2019), and 5) thermal properties (Hofmeister, 2014; Horai, 1971; Saxena et al., 2012; Zhu et al., 2019). Importantly, using structure search and *ab initio* calculations (Hermann and Mookherjee, 2016) predicted that brucite is stable along the *P-T* conditions of a subducting slab until about 30 GPa (~800 km depth), after which it decomposes to periclase (MgO) and H_2O. The stability of brucite would impact the relative stability of other minerals in the MSH system (Hacker et al., 2003; Ohtani et al., 2000; Ohtani et al., 1995). Potentially the drastic changes in physical properties across brucite's decomposition to periclase and H_2O could trigger local seismic and geodynamic anomalies (see Hermann and Mookherjee (2016) and our discussion below).

Lattice thermal conductivity, the ability of a material to conduct heat, of minerals in the mantle and subducting slabs is crucial to control the thermal evolution and geodynamics in Earth's interior (Chang et al., 2017; Dalton et al., 2013; Deschamps and Hsieh, 2019; Hsieh et al., 2017; Hsieh et al., 2018; Hsieh et al., 2020; Marzotto et al., 2020). Recent studies suggested that a temperature anomaly within a subducting slab could be induced by large variations of thermal conductivity in the oceanic crust due to, for instance, the effect of hydration (Chang et al., 2017) or spin transition (Chao and Hsieh, 2019; Hsieh et al., 2020). Since brucite could coexist with phase D in the

peridotitic layer of a subducting slab, yet decompose to periclase in the shallow lower mantle, how the thermal conductivity changes across the decomposition could critically influence the local temperature profile, the stability of other hydrous minerals, and dynamics of slabs. Prior studies on the brucite thermal conductivity have been limited to polycrystalline or powder samples (Hofmeister, 2014; Horai, 1971; Yagi et al., 2010). However, at ambient conditions brucite is a layered crystal ($P\bar{3}$ symmetry) with large elastic anisotropy (Hermann and Mookherjee, 2016). Knowledge to the thermal conductivity of brucite along different crystal orientations under extreme conditions is critically needed as it could offer novel insights to the thermal profiles of a slab and ambient mantle, with important consequences on slab's subduction dynamics and route of water cycle in the shallow lower mantle.

In this work, we coupled ultrafast time-domain thermoreflectance with diamond-anvil cells (DAC) to study the lattice thermal conductivity of brucite along *a*- ([100]) and *c*-axis ([001]) of the crystal to 30 GPa. We observed a strong thermal conductivity anisotropy that reduces with pressure. Our modeled thermal conductivity profiles of the brucite and periclase along a slab's geotherm further indicate a significant increase in the thermal conductivity by ~6–19 folds, depending on brucite's crystal orientation, at depth of ~800 km. The large thermal conductivity discontinuity across the decomposition of

91 brucite to periclase suggests that a local high-temperature anomaly can be induced as the
92 brucite-rich aggregate within a slab is subducted to the shallow lower mantle and
93 eventually decomposed, enhancing slab's buoyancy for stagnation and release of water in
94 the region. Similar to the endothermic ringwoodite to bridgmanite and ferropericlase
95 transition at ~660 km depth that increases slab's buoyancy (Goes et al., 2017), the
96 decomposition of brucite at ~800 km depth not only creates additional effective mantle
97 resistance that impacts the slab dynamics, but serves as a new water source that promotes
98 formation of dehydration melts, causing seismic low velocities in the shallow lower
99 mantle.
100

101 ## Experimental Methods

102 ### Starting materials and sample preparation

103 Natural samples of brucite used in this study were collected from Killa Saifullah
104 District in Balochistan, Pakistan. Their chemical composition was confirmed to be
105 $Mg(OH)_2$ using energy-dispersive X-ray spectroscopy with an Oxford X max-80 detector.
106 We determined the crystal orientation along the [100] and [001] axes with single-crystal
107 X-ray diffraction (Bruker X8 APEX). To perform thermal conductivity measurements
108 under high pressures, we first polished each brucite sample down to a thickness of ~30

μm and coated an ~90 nm thick aluminum (Al) film on the brucite. We then loaded the sample, along with a ruby sphere, into a symmetric piston-cylinder DAC with a culet size of 400 μm and a tungsten gasket. We used silicone oil (CAS No. 63148-62-9 from ACROS ORGANICS) as the pressure medium. The schematic illustration of the brucite sample within a DAC is shown in Fig. 1. We measured the pressure within the sample chamber using calibrated ruby fluorescence (Mao et al., 1986), which has a typical uncertainty of less than 5% within the pressure range we studied, from ambient to 30 GPa.

Lattice thermal conductivity measurements

We measured the lattice thermal conductivity of brucite using time-domain thermoreflectance (TDTR). TDTR is an ultrafast optical technique which uses a mode-locked, 785-nm wavelength, Ti:sapphire laser to pump and probe thermal diffusion through a material. The output of the laser was split into pump and probe beams that were both focused onto the Al film coated on the sample. We used the pump beam to heat up the Al film and then used the probe beam to measure the resulting optical reflectivity change on the Al film due to the temperature variations over time (Fig. 1). We measured the in-phase (V_{in}) and out-of-phase (V_{out}) components of variations in the reflected probe

beam intensity using a silicon photodiode and lock-in amplifier. Detailed descriptions of the TDTR technique are available in Cahill (2004) and Hsieh et al. (2009).

To derive the thermal conductivity of the brucite sample, we compared the ratio of V_{in} to V_{out} ($-V_{in}/V_{out}$) as a function of delay time between the pump and probe beams to the numerical calculations of a bi-directional heat-flow model (Ge et al., 2006; Schmidt et al., 2008), see Fig. 2 for an example of TDTR data compared with model calculations. Table 1 contains the input parameters for the heat-flow model for Fig. 2, including laser spot size, Al-film thickness, and the thermal conductivity and volumetric heat capacity of each layer (i.e., silicone oil, Al film, and brucite). As such, the brucite thermal conductivity is the only significant, free parameter in the model, which is determined by manipulating it until the model calculation matches the experimental data with the minimum mean-square error (Fig. 2). We measured the thickness of Al film at ambient conditions using picosecond acoustics (O'Hara et al., 2001) and estimated the changes in thickness as a function of pressure using the equation-of-state of Al following a method developed in (Chen et al., 2011). Since the thermal penetration depths (the skin depth that a heat wave can diffuse into a material) of the silicone oil and brucite sample are both only on the order of few hundred nanometers (Hsieh et al., 2009), the heat-flow model calculations are not sensitive to their thicknesses. The thermal conductivity and heat

capacity of silicone oil and Al as a function of pressure were taken from previous data (Hsieh, 2015; Hsieh et al., 2009). The volumetric heat capacity of brucite at ambient conditions is 3.12 J cm^{-3} K^{-1} (Saxena et al., 2012); we assumed it is a constant under high pressure because upon compression the decrease in brucite's specific heat per molecule is largely counterbalanced by the increase in its density (Hermann and Mookherjee, 2016; Xia et al., 1998). Figure 2 also shows that the estimated uncertainty of each of the parameters in the heat-flow model (Table 1) propagates an integrated error in the measured brucite thermal conductivity of approximately 5% at ambient pressure and about 20% at 30 GPa.

Experimental Results

Thermal conductivity at high pressure and room temperature

Figure 3(a) shows the brucite thermal conductivity (Λ) along the [100] ($\Lambda_{[100]}$) and [001] ($\Lambda_{[001]}$) axes under high pressure and room temperature. At ambient conditions, the $\Lambda_{[100]}$ and $\Lambda_{[001]}$ are 12.6 ± 0.11 W m^{-1} K^{-1} and 1.08 ± 0.08 W m^{-1} K^{-1}, respectively, resulting in a large conductivity ratio ($\Lambda_{[100]}/\Lambda_{[001]}$) of 11.7, which indicates a significant conductivity anisotropy between the crystal axes. Literature data for the polycrystalline brucite at ambient conditions from Horai (1971) (open triangles in Fig. 3(a)) are plotted

for comparison, which fall within the range between $\Lambda_{[100]}$ and $\Lambda_{[001]}$. As the pressure increases, the $\Lambda_{[100]}$ and $\Lambda_{[001]}$ increase as a function of pressure, reaching 20.7 ± 2.3 W m^{-1} K^{-1} and 6.3 ± 0.8 W m^{-1} K^{-1} at 30 GPa, respectively, with a conductivity ratio reducing to about 3.3. The pressure dependence of $\Lambda_{[100]}$ and $\Lambda_{[001]}$ up to 30 GPa form an upper and lower bound, respectively, for the thermal conductivity of brucite. Importantly, during slab subduction, lattice preferred orientation (LPO) could be present in minerals around the interface of slab and mantle, such as in serpentine and talc (Mookherjee and Capitani, 2011). If the LPO exists in brucite whose thermal conductivity is highly anisotropic (Fig. 3(a)), the heat transfer through the slab could be substantially affected by which axis of brucite that preferentially orients parallel to the direction of slab motion.

Moreover, Hermann and Mookherjee (2016) predicted that brucite undergoes a phase transition from $P\bar{3}$ to $P4_12_12$ at ~22 GPa and room temperature. Our data show that only the $\Lambda_{[100]}$ presents a small kink coincidentally around 20–23 GPa, which, however, is comparable to the measurement errors. We thus conclude that the potential $P\bar{3}$ to $P4_12_12$ transition, if exists, does not significantly alter the brucite thermal conductivity.

In order to estimate the thermal conductivity of brucite under slab's high *P*-*T* conditions (see our discussion below), here we first parameterized the pressure

dependences of $\Lambda_{[100]}$ and $\Lambda_{[001]}$ (Fig. 3(a)) based on the best-fit third-order-polynomial regression (blue and orange dotted curves in Fig. 3(a)):

$$\Lambda(P) = (\Lambda_{amb}+aP+bP^2+cP^3), \quad (1)$$

where Λ_{amb} is the thermal conductivity at ambient conditions and a, b, and c are the linear, quadratic, and cubic coefficients, respectively. The parameterization coefficients for $\Lambda_{[100]}$ and $\Lambda_{[001]}$ are listed in Table 2.

Thermal conductivity at elevated temperature and ambient pressure

In addition to the high-pressure and room-temperature measurements, to understand the effect of temperature on brucite thermal conductivity, we have also performed TDTR measurements at elevated temperature (up to ~480 K) and ambient pressure, see Fig. 3 (b). Both $\Lambda_{[100]}$ and $\Lambda_{[001]}$ substantially decrease with increasing temperature, for instance, by ~50% at ~480 K. Note that higher temperature results in a degradation of Al film quality and thus a deterioration in measurement integrity. Though our measurement temperature was limited up to ~480 K, temperature dependences of the $\Lambda_{[100]}$ and $\Lambda_{[001]}$ were clearly observed. We fit the data for $\Lambda_{[100]}$ and $\Lambda_{[001]}$ to a power relationship (dashed curves in Fig. 3(b) (Chang et al., 2017; Hofmeister, 1999; Xu et al., 2004; Zhang et al., 2019)), i.e.,

$$\Lambda(T) = \Lambda_{amb}(298/T)^n, \quad (2)$$

where T is the temperature (K) and Λ_{amb} the thermal conductivity at ambient conditions. We find that the exponent, n, equals 0.83 ± 0.17 and 0.88 ± 0.24 for the [100] and [001] orientation, respectively. These values of n are in good agreement with previous results for pure materials, whose thermal conductivity typically follows a T^{-1} dependence (Dalton et al., 2013; Hofmeister, 1999; Klemens et al., 1962; Zhang et al., 2019). The slight deviation of our n values from the ideal value (n=1) could be caused by the large amounts of hydroxyl (OH^-) in brucite which act as impurities to enhance phonon scattering, similar to the roles that iron plays in many iron-bearing minerals (Chang et al., 2017; Xu et al., 2004; Zhang et al., 2019).

Discussions and Geophysical Impacts

Hacker et al. (2003) suggested that brucite could make up a significant portion (10–15 vol%) of depleted lherzolite and harzburgite, which are the abundant rock compositions relevant to a subducting hydrous crust. Mineral physics experiments (Irifune et al., 1998; Ohtani et al., 2000; Ohtani et al., 1995) have shown that brucite could coexist with phase D at pressures of ~19–27 GPa and temperatures of ~900–1200 K, coinciding with the typical geotherm of a subducting slab at ~600–800 km depth. Our

results for the pressure-temperature evolution of brucite thermal conductivity (Fig. 3) offer insights into not only its potential impacts on the thermal state around a subduction zone, but also on the occurrence of slab stagnation in the shallow lower mantle. Although the brucite may not be a major mineral phase in the Earth's interior, it could be locally concentrated within a cold and wet subducting slab (Irifune et al., 1998; Ohtani et al., 1995). As such, it could still play a significant role since the effective thermal conductivity of the slab materials largely depends on how the brucite is distributed within the aggregate and on the effect of its decomposition to periclase.

Thermal conductivity discontinuity as brucite decomposes to periclase

To understand the potential temperature anomaly triggered by the decomposition of brucite to periclase, we used the *P*-*T* dependences of brucite thermal conductivity (equations (1) and (2)) to model the $\Lambda_{[100]}$ and $\Lambda_{[001]}$ of brucite along a representative geotherm of a subducting slab (Eberle et al., 2002), see the blue and orange curves in Fig. 4, respectively. Interestingly, both the $\Lambda_{[100]}$ and $\Lambda_{[001]}$ are weakly dependent on the depth, reaching ~6.7 and 2.0 W m^{-1} K^{-1}, respectively, at ~800 km depth (~30 GPa) where it is expected to decompose to periclase (Hermann and Mookherjee, 2016). For the periclase thermal conductivity profile (green curve in Fig. 4), we took the literature data from

Dalton et al. (2013) and assumed its thermal conductivity follows a typical T^{-1} dependence (Dalton et al., 2013; Hofmeister, 1999; Klemens et al., 1962; Zhang et al., 2019) along the same slab geotherm. At ~800 km depth, the thermal conductivity of periclase increases to ~38 W m^{-1} K^{-1}, much larger than those of brucite along [100] and [001] by a factor of ~6 and 19, respectively. This implies that as the brucite is locally enriched within a slab and subducted to the depth of ~800 km, the decomposition to periclase could result in a significant discontinuity in the effective thermal conductivity at the peridotite layer of the slab, where brucite is locally enriched. We note that the phase diagram of brucite by (Fukui et al., 2005) suggested that at a temperature of ~1000 K (typical slab geotherm around the top of lower mantle (Eberle et al., 2002; Hermann and Mookherjee, 2016)), the brucite would decompose to periclase at pressures of ~25 GPa (~660 km), i.e., slightly shallower depth than the 800 km. Nevertheless, the thermal conductivity discontinuity induced by brucite decomposition along with its geophysical impacts, including a potential high-temperature anomaly which promotes slab stagnation and release of water in the shallow lower mantle, remains the same (see our discussions below).

It should also be noted that water, either as a liquid or ice VII, may also be a product of this decomposition (Fukui et al., 2005; Hermann and Mookherjee, 2016), which could

affect the local thermal conductivity. However, the lower viscosity and density of the water will allow it to migrate out of the peridotite layer rapidly enough that its effect should be minimal (Abramson, 2007; Bina and Navrotsky, 2000).

Potential local high-temperature anomaly promotes slab stagnation in the shallow lower mantle

Global seismic tomography has revealed three main behaviors of subducting slabs in different regions: 1) stagnation at the bottom of the mantle transition zone (~660 km depth); 2) stagnation in the shallow lower mantle (~800–1000 km depth); and 3) further penetration into the lower mantle, potentially reaching the core-mantle boundary (Čížková and Bina, 2019; Fukao and Obayashi, 2013; Fukao et al., 2009; Lee and King, 2011). Several mechanisms or effects have been proposed to account for such different slab subduction dynamics and causes of slab stagnation. The mechanisms include, for instance, the negative Clapeyron slope at 660 km depth (Ballmer et al., 2015; Mao and Zhong, 2018; Torii and Yoshioka, 2007), a drastic increase in the ambient mantle viscosity (Alpert et al., 2010; Ballmer et al., 2015; Čížková and Bina, 2019; Mao and Zhong, 2018; Marquardt and Miyagi, 2015), fraction of basalt in pyrolitic mantle (Ballmer et al., 2015), trench retreat, and slab's age and dipping angle (Christensen, 1996;

Goes et al., 2017; Mao and Zhong, 2018), etc.

Mechanisms that flatten a sinking slab in the shallow lower mantle (~800–1000 km depth), however, remain poorly understood as there is no major phase transition of lower mantle minerals within such depth range. Based on the analysis of the long wavelengths of the geoid, (Rudolph et al., 2015) found an increase in mantle viscosity in the depth range of ~800–1200 km that may result in the slab stagnation around this depth range. On the other hand, as we discussed before, the temperature profiles in the mantle and subduction zones are a key parameter to control their density, viscosity, and buoyancy with crucial consequences on the slab dynamics. As such, it is intuitive that the slab thermal conductivity, which controls heat flow into the slab, will be an important factor in understanding the causes of slab stagnation.

If the brucite is locally concentrated in a subducting slab and transported to the shallow lower mantle of ~800 km depth and eventually decomposed, the drastic increase in the brucite-rich aggregate thermal conductivity (~6–19 folds) triggered by the brucite decomposition to periclase would considerably enhance the heat transfer from the surrounding mantle into the slab, leading to a local high-temperature anomaly at the core of the slab. Though the decomposition reaction may increase the slab density, it is relatively small amount and localized at the top of the slab. The rise of temperature

through the slab, in turn, reduces the slab's density and viscosity, and enhances its buoyancy, hindering the descent of the subducting slab to deeper lower mantle (see the red shaded region within the slab in Fig. 4). Similar to the endothermic ringwoodite to bridgmanite and ferropericlase transition at ~660 km depth that absorbs heat and increases slab's buoyancy (Goes et al., 2017), the scenario by brucite decomposition offers a new mechanism to additionally enhance the effective mantle resistance at ~800 km depth that could, at least partially, contribute to the stagnation of slabs in the shallow lower mantle as observed by tomographic images.

An additional water source to promote low-velocity zones at the top of lower mantle

In addition to the slab stagnation, seismic tomography has also imaged seismic low-velocity zones (LVZs) at the top of lower mantle, ~700–800 km depth, see, e.g., (Fukao and Obayashi, 2013; Schmandt et al., 2014). Mineral physics experiments coupled with electrical conductivity measurements and geodynamics modelling suggest that the LVZs at the top of lower mantle may be associated with the formation of partial melts assisted by hydrous fluids released either from the hydrous ringwoodite-bridgmanite phase transition as the mantle flows downward across the 660 km discontinuity, or from the decomposition of dense hydrous magnesium silicates (DHMS), e.g., superhydrous phase

B and phase D (Karato, 2011; Ohtani, 2015; Ohtani et al., 2018; Schmandt et al., 2014).

The hydrous minerals in the peridotite layer of a subducting slab undergo a series of phase transitions during subduction, in which phase D along with brucite could coexist at the *P*-*T* conditions of a subducting slab at ~600–800 km depth (Irifune et al., 1998; Ohtani, 2005; Ohtani, 2015; Ohtani et al., 2018). In addition to the DHMS that can release water via dehydration, brucite, which contains large amounts of water (~30 wt%), could also serve as a water source to facilitate the formation of partial melt, leading to the seismic anomalies in the region: when the brucite-rich aggregate is subducted to ~800 km depth, the decomposition process releases H_2O that can migrate upwards (see the schematic illustration in Fig. 4) due to its lower density and viscosity (Abramson, 2007), additionally contributing water accumulation around the top of lower mantle. Moreover, the local high-temperature anomaly induced by brucite decomposition to periclase would help destabilize other co-existing hydrous minerals (e.g., phase D) and enhance their dehydration, releasing more water to the ambient mantle. As an additional water source and driver for local higher temperature anomalies, brucite decomposition provides a novel mechanism for the formation of the LVZs at the top of lower mantle with broader implications for the route and budget of the deep water cycle.

Implications

Combination of our novel experimental results with data modeling enables us to infer that upon its decomposition, the brucite-rich aggregate within a sinking slab could create a local thermal anomaly, influencing not only slab's subduction dynamics, but also the stability field of minerals and seismic structures in surrounding mantle. Such effects are expected to be general since the hydrous minerals in a sinking slab undergo a series of phase transitions during subduction. Therefore, future experimental studies on the thermal conductivity of other prominent hydrous minerals, such as a series of DHMS, under relevant *P*-*T* conditions may uncover additional thermal conductivity discontinuities present across phase transitions. An improved understanding of this thermal conductivity framework has important implications for the local thermal states and the mantle and subducting slab's dynamics. Further combination of our experimental findings and numerical thermo-chemical modelling will significantly advance our understanding of the thermo-chemical structures of subduction zones and their effects on the budget and route of Earth's deep water transportation.

Acknowledgments

This work was supported by the Academia Sinica and the Ministry of Science and

Technology (MOST) of Taiwan, Republic of China, under Contract AS-CDA-106-M02, 106-2116-M-001-022, and 107-2628-M-001-004-MY3. WPH acknowledges the fellowship from the Foundation for the Advancement of Outstanding Scholarship, Taiwan. We also thank Yoshiyuki Iizuka, Dylan W. Meyer, Yuh-Sheng Wen, Chao-Chih Chen, Yi-Chi Tsao, and Yu-Shiang Wang of Academia Sinica for their help with the experiments and helpful comments.

References

Abramson, E.H. (2007) Viscosity of water measured to pressures of 6 GPa and temperatures of 300 °C. Physical Review E, 76(5), 051203.

Alpert, L., Becker, T., and Bailey, I. (2010) Global slab deformation and centroid moment tensor constraints on viscosity. Geochemistry, Geophysics, Geosystems, 11(12), 1-22.

Ballmer, M.D., Schmerr, N.C., Nakagawa, T., and Ritsema, J. (2015) Compositional mantle layering revealed by slab stagnation at ~1000-km depth. Science Advances, 1(11), e1500815.

Bina, C.R., and Navrotsky, A. (2000) Possible presence of high-pressure ice in cold subducting slabs. Nature, 408(6814), 844-847.

Čížková, H., and Bina, C.R. (2019) Linked influences on slab stagnation: Interplay between lower mantle viscosity structure, phase transitions, and plate coupling. Earth and Planetary Science Letters, 509, 88-99.

Cahill, D.G. (2004) Analysis of heat flow in layered structures for time-domain thermoreflectance. Review of scientific instruments, 75(12), 5119-5122.

Catti, M., Ferraris, G., Hull, S., and Pavese, A. (1995) Static compression and H disorder in brucite, $Mg(OH)_2$, to 11 GPa: a powder neutron diffraction study. Physics and Chemistry of Minerals, 22(3), 200-206.

Chang, Y.-Y., Hsieh, W.-P., Tan, E., and Chen, J. (2017) Hydration-reduced lattice thermal conductivity of olivine in Earth's upper mantle. Proceedings of the

National Academy of Sciences, 114(16), 4078-4081.

Chao, K.-H., and Hsieh, W.-P. (2019) Thermal conductivity anomaly in $(Fe_{0.78}Mg_{0.22})CO_3$ siderite across spin transition of Iron. Journal of Geophysical Research: Solid Earth, 124(2), 1388-1396.

Chen, B., Hsieh, W.-P., Cahill, D., Trinkle, D., and Li, J. (2011) Thermal conductivity of compressed H_2O to 22 GPa: a test of the Leibfried-Schlömann equation. Phys. Rev. B, 83(13), 132301.

Christensen, U.R. (1996) The influence of trench migration on slab penetration into the lower mantle. Earth and Planetary Science Letters, 140(1-4), 27-39.

Dalton, D.A., Hsieh, W.-P., Hohensee, G.T., Cahill, D.G., and Goncharov, A.F. (2013) Effect of mass disorder on the lattice thermal conductivity of MgO periclase under pressure. Scientific Reports, 3, 2400.

Deschamps, F., and Hsieh, W.-P. (2019) Lowermost mantle thermal conductivity constrained from experimental data and tomographic models. Geophysical Journal International, 219, S115-S136.

Duffy, T.S., Meade, C., Fei, Y., Mao, H.-K., and Hemley, R.J. (1995) High-pressure phase transition in brucite, $Mg(OH)_2$. American Mineralogist, 80(3-4), 222-230.

Eberle, M.A., Grasset, O., and Sotin, C. (2002) A numerical study of the interaction between the mantle wedge, subducting slab, and overriding plate. Physics of the Earth and Planetary Interiors, 134(3-4), 191-202.

Fukao, Y., and Obayashi, M. (2013) Subducted slabs stagnant above, penetrating through, and trapped below the 660 km discontinuity. Journal of Geophysical Research: Solid Earth, 118(11), 5920-5938.

Fukao, Y., Obayashi, M., Nakakuki, T., and Deep Slab Project Group. (2009) Stagnant slab: a review. Annual Review of Earth and Planetary Sciences, 37, 19-46.

Fukui, H., Inoue, T., Yasui, T., Katsura, T., Funakoshi, K.-I., and Ohtaka, O. (2005) Decomposition of brucite up to 20 GPa: Evidence for high MgO-solubility in the liquid phase. European journal of mineralogy, 17(2), 261-267.

Ge, Z., Cahill, D.G., and Braun, P.V. (2006) Thermal conductance of hydrophilic and hydrophobic interfaces. Physical review letters, 96(18), 186101.

Goes, S., Agrusta, R., van Hunen, J., and Garel, F. (2017) Subduction-transition zone interaction: a review. Geosphere, 13(3), 644-664.

Hacker, B.R., Abers, G.A., and Peacock, S.M. (2003) Subduction factory 1. Theoretical mineralogy, densities, seismic wave speeds, and H_2O contents. Journal of Geophysical Research: Solid Earth, 108(B1), 1-26.

Hermann, A., and Mookherjee, M. (2016) High-pressure phase of brucite stable at Earth's

mantle transition zone and lower mantle conditions. Proceedings of the National Academy of Sciences, 113(49), 13971-13976.

Hofmeister, A. (1999) Mantle values of thermal conductivity and the geotherm from phonon lifetimes. Science, 283(5408), 1699-1706.

Hofmeister, A. (2014) Thermal diffusivity and thermal conductivity of single-crystal MgO and Al_2O_3 and related compounds as a function of temperature. Physics and Chemistry of Minerals, 41(5), 361-371.

Horai, K.-i. (1971) Thermal conductivity of rock-forming minerals. Journal of Geophysical Research, 76(5), 1278-1308.

Hsieh, W.-P. (2015) Thermal conductivity of methanol-ethanol mixture and silicone oil at high pressures. Journal of Applied Physics, 117(23), 235901.

Hsieh, W.-P., Chen, B., Li, J., Keblinski, P., and Cahill, D.G. (2009) Pressure tuning of the thermal conductivity of the layered muscovite crystal. Physical Review B, 80(18), 180302.

Hsieh, W.-P., Deschamps, F., Okuchi, T., and Lin, J.-F. (2017) Reduced lattice thermal conductivity of Fe-bearing bridgmanite in Earth's deep mantle. Journal of Geophysical Research: Solid Earth, 122(7), 4900-4917.

Hsieh, W.-P., Deschamps, F., Okuchi, T., and Lin, J.-F. (2018) Effects of iron on the lattice thermal conductivity of Earth's deep mantle and implications for mantle dynamics. Proceedings of the National Academy of Sciences, 115(16), 4099-4104.

Hsieh, W.-P., Ishii, T., Chao, K.-H., Tsuchiya, J., Deschamps, F., and Ohtani, E. (2020) Spin transition of iron in δ-(Al,Fe)OOH induces thermal anomalies in Earth's lower mantle. Geophysical Research Letters, 47(4), e2020GL087036.

Irifune, T., Kubo, N., Isshiki, M., and Yamasaki, Y. (1998) Phase transformations in serpentine and transportation of water into the lower mantle. Geophysical Research Letters, 25(2), 203-206.

Jiang, F., Speziale, S., and Duffy, T.S. (2006) Single-crystal elasticity of brucite, $Mg(OH)_2$, to 15 GPa by Brillouin scattering. American Mineralogist, 91(11-12), 1893-1900.

Karato, S.-i. (2011) Water distribution across the mantle transition zone and its implications for global material circulation. Earth and Planetary Science Letters, 301(3-4), 413-423.

Klemens, P., White, G., and Tainsh, R. (1962) Scattering of lattice waves by point defects. Philosophical Magazine, 7(80), 1323-1335.

Kruger, M., Williams, Q., and Jeanloz, R. (1989) Vibrational spectra of $Mg(OH)_2$ and

$Ca(OH)_2$ under pressure. The Journal of Chemical Physics, 91(10), 5910-5915.

Lee, C., and King, S.D. (2011) Dynamic buckling of subducting slabs reconciles geological and geophysical observations. Earth and Planetary Science Letters, 312(3-4), 360-370.

Mainprice, D., and Ildefonse, B. (2009) Seismic anisotropy of subduction zone minerals–contribution of hydrous phases. In S. Lallemand, and F. Funiciello, Eds. Subduction zone geodynamics, p. 63-84. Springer, Berlin, Heidelberg.

Mao, H., Xu, J.-A., and Bell, P. (1986) Calibration of the ruby pressure gauge to 800 kbar under quasi-hydrostatic conditions. Journal of Geophysical Research: Solid Earth, 91(B5), 4673-4676.

Mao, W., and Zhong, S. (2018) Slab stagnation due to a reduced viscosity layer beneath the mantle transition zone. Nature Geoscience, 11(11), 876-881.

Marquardt, H., and Miyagi, L. (2015) Slab stagnation in the shallow lower mantle linked to an increase in mantle viscosity. Nature Geoscience, 8(4), 311-314.

Marzotto, E., Hsieh, W.-P., Ishii, T., Chao, K.-H., Golabek, G.J., Thielmann, M., and Ohtani, E. (2020) Effect of water on lattice thermal conductivity of ringwoodite and its implications for the thermal evolution of descending slabs. Geophysical Research Letters, 47(13), e2020GL087607.

Mookherjee, M., and Capitani, G.C. (2011) Trench parallel anisotropy and large delay times: Elasticity and anisotropy of antigorite at high pressures. Geophysical Research Letters, 38(9), 1-6.

Mookherjee, M., and Stixrude, L. (2006) High-pressure proton disorder in brucite. American Mineralogist, 91(1), 127-134.

Nagai, T., Hattori, T., and Yamanaka, T. (2000) Compression mechanism of brucite: an investigation by structural refinement under pressure. American Mineralogist, 85(5-6), 760-764.

Nishi, M., Irifune, T., Tsuchiya, J., Tange, Y., Nishihara, Y., Fujino, K., and Higo, Y. (2014) Stability of hydrous silicate at high pressures and water transport to the deep lower mantle. Nature Geoscience, 7(3), 224-227.

O'Hara, K., Hu, X., and Cahill, D.G. (2001) Characterization of nanostructured metal films by picosecond acoustics and interferometry. Journal of Applied Physics, 90(9), 4852-4858.

Ohtani, E. (2005) Water in the mantle. Elements, 1(1), 25-30.

Ohtani, E. (2015) Hydrous minerals and the storage of water in the deep mantle. Chemical Geology, 418, 6-15.

Ohtani, E., Mizobata, H., and Yurimoto, H. (2000) Stability of dense hydrous magnesium

silicate phases in the systems Mg_2SiO_4 -H_2O and $MgSiO_3$ -H_2O at pressures up to 27 GPa. Physics and Chemistry of Minerals, 27(8), 533-544.

Ohtani, E., Shibata, T., Kubo, T., and Kato, T. (1995) Stability of hydrous phases in the transition zone and the upper most part of the lower mantle. Geophysical Research Letters, 22(19), 2553-2556.

Ohtani, E., Yuan, L., Ohira, I., Shatskiy, A., and Litasov, K. (2018) Fate of water transported into the deep mantle by slab subduction. Journal of Asian Earth Sciences, 167, 2-10.

Parise, J.B., Leinenweber, K., Weidnner, D.J., Tan, K., and Von Dreele, R.B. (1994) Pressure-induced H bonding: Neutron diffraction study of brucite, $Mg(OD)_2$, to 9.3 GPa. American Mineralogist, 79(1-2), 193-196.

Pawley, A.R., and Wood, B.J. (1996) The low-pressure stability of phase A, $Mg_7Si_2O_8(OH)_6$. Contributions to Mineralogy and Petrology, 124(1), 90-97.

Raugei, S., Silvestrelli, P.L., and Parrinello, M. (1999) Pressure-induced frustration and disorder in $Mg(OH)_2$ and $Ca(OH)_2$. Physical Review Letters, 83(11), 2222-2225.

Rudolph, M.L., Lekić, V., and Lithgow-Bertelloni, C. (2015) Viscosity jump in Earth's mid-mantle. Science, 350(6266), 1349-1352.

Saxena, S.K., Chatterjee, N., Fei, Y., and Shen, G. (2012) Thermodynamic data on oxides and silicates: an assessed data set based on thermochemistry and high pressure phase equilibrium. 322-323 p. Springer Science & Business Media.

Schmandt, B., Jacobsen, S.D., Becker, T.W., Liu, Z., and Dueker, K.G. (2014) Dehydration melting at the top of the lower mantle. Science, 344(6189), 1265-1268.

Schmidt, A., Chiesa, M., Chen, X., and Chen, G. (2008) An optical pump-probe technique for measuring the thermal conductivity of liquids. Review of Scientific Instruments, 79(6), 064902.

Torii, Y., and Yoshioka, S. (2007) Physical conditions producing slab stagnation: Constraints of the Clapeyron slope, mantle viscosity, trench retreat, and dip angles. Tectonophysics, 445(3-4), 200-209.

Xia, X., Weidner, D., and Zhao, H. (1998) Equation of state of brucite: Single-crystal Brillouin spectroscopy study and polycrystalline pressure-volume-temperature measurement. American Mineralogist, 83(1), 68-74.

Xu, Y., Shankland, T.J., Linhardt, S., Rubie, D.C., Langenhorst, F., and Klasinski, K. (2004) Thermal diffusivity and conductivity of olivine, wadsleyite and ringwoodite to 20 GPa and 1373 K. Physics of the Earth and Planetary Interiors, 143, 321-336.

Yagi, T., Ohta, K., Kobayashi, K., Taketoshi, N., Hirose, K., and Baba, T. (2010) Thermal diffusivity measurement in a diamond anvil cell using a light pulse thermoreflectance technique. Measurement Science and Technology, 22(2), 024011.

Zhang, Y., Yoshino, T., Yoneda, A., and Osako, M. (2019) Effect of iron content on thermal conductivity of olivine with implications for cooling history of rocky planets. Earth and Planetary Science Letters, 519, 109-119.

Zhu, X., Guo, X., Smyth, J.R., Ye, Y., Wang, X., and Liu, D. (2019) High-temperature vibrational spectra between $Mg(OH)_2$ and $Mg(OD)_2$: Anharmonic contribution to thermodynamics and D/H fractionation for brucite. Journal of Geophysical Research: Solid Earth, 124(8), 8267-8280.

List of figure captions

Figure 1. Schematic illustration of the optical pump-probe measurements coupled with a diamond-anvil cell (left panel), and an optical microscopic image of the brucite within the diamond-anvil cell (right panel). The brucite sample is coated with an Al thin film that serves as a transducer to absorb heat from the pump beam and to enable measurements of temperature through changes in optical reflectivity. The pressure medium is silicone oil. The pressure is measured by ruby fluorescence.

Figure 2. Example time-domain thermoreflectance spectrum of brucite along the [100] axis at (**a**) ambient conditions and (**b**) 30.33 GPa and room temperature, along with the heat-flow model calculations. Open symbols show the experimental data for the ratio (-

V_{in}/V_{out}) as a function of delay time. Brucite thermal conductivities of 11.5 W m^{-1} K^{-1} at ambient pressure and 20.0 W m^{-1} K^{-1} at 30.33 GPa provide best-fits to the data, assuming the input parameters listed in Table 1. Red curves represent the best fit to the data with the minimum value of mean-square error (MSE). The blue and light green dashed curves represent the ± 5% and ± 20% uncertainty at ambient pressure and 30.33 GPa, respectively.

Figure 3. (**a**) Pressure dependence of the thermal conductivity of brucite along [100] (blue circles) and [001] (orange squares) at room temperature. Several runs of measurements yield consistent results. Blue and orange dotted curves are third-order polynomial fits to the data (see text for details). Literature data for polycrystalline brucite at ambient conditions (open triangles) (Horai, 1971) are plotted for comparison. (**b**) Temperature dependence of the thermal conductivity of brucite along [100] (blue circles) and [001] (orange squares) at ambient pressure. Blue and orange dashed curves are the best fits for each dataset according to a temperature-dependent power regression, $\Lambda(T) = \Lambda_{amb}(298/T)^n$, where n =0.83 ± 0.17 and 0.88 ± 0.24 for [100] and [001], respectively.

Figure 4. Modeled thermal conductivity profiles of brucite (blue and orange curves for

[100] and [001], respectively) and periclase (green curve) along a typical cold slab geotherm (Eberle et al., 2002) and a schematic illustration of brucite-rich aggregate in a slab subducted to ~800 km depth. The large thermal conductivity discontinuity (dotted arrow, ~6–19-fold increase) through the decomposition of brucite to periclase could trigger a local high-temperature (T) anomaly within the slab (red shaded region), which decreases slab's viscosity (η) and density (ρ), while increases its buoyancy. These effects offer a novel mechanism to promote slab stagnation around 800 km depth. Moreover, the water released from brucite decomposition (blue droplets) would migrate upward to the uppermost lower mantle (~700–800 km depth) and facilitate the formation of dehydration melt, resulting in a seismic low-velocity zone (LVZ).

Table 1. Input parameters used in the heat-flow model for brucite along the [100] axis at ambient conditions and at 30.33 GPa and room temperature.

Model Parameters (unit)		Pressure (GPa)	
		10^{-4}	30.33
r^a	(μm)	7.6	7.6
$C_{brucite}{}^b$	(J cm^{-3} K^{-1})	3.12	3.12
$C_{Al}{}^c$	(J cm^{-3} K^{-1})	2.42	2.66
$C_{Si}{}^d$	(J cm^{-3} K^{-1})	N/A	1.4
$\Lambda_{Al}{}^e$	(W m^{-1} K^{-1})	200	200
$\Lambda_{Si}{}^f$	(W m^{-1} K^{-1})	N/A	1.753
$h_{brucite}{}^g$	(μm)	30	30
$h_{Al}{}^h$	(nm)	84.61	91.98
$h_{Si}{}^i$	(μm)	N/A	10
G^j	(MW m^{-2} K^{-1})	43	182

[a]Laser spot size (in radius, measured in this study). [b]Volumetric heat capacity of brucite (Saxena et al., 2012), which was assumed to only depend on temperature, not pressure. [c]Volumetric heat capacity of Al (Hsieh et al., 2009). [d]Volumetric heat capacity of silicone oil (Hsieh, 2015). [e]Thermal conductivity of Al (Hsieh et al., 2009). [f]Thermal conductivity of silicone oil (Hsieh, 2015). [g]Thickness of brucite sample. [h]Thickness of Al film (measured at ambient pressure using picosecond acoustics). [i]Thickness of silicone oil layer between diamond anvil and sample. [j]Thermal conductance at Al-brucite and Al-silicone oil interfaces. Note that for measurements at ambient pressure, the silicone oil was not used and thus its heat capacity, thermal conductivity, and thickness were not taken into account in the heat-flow model.

568

569

Table 2. Parameterization coefficients for $\Lambda(P) = (\Lambda_{amb}+aP+bP^2+cP^3)$ to fit the brucite thermal conductivity data in Figure 3(**a**).

Minerals	Λ_{amb}	**a**	**b (10^{-2})**	**c (10^{-4})**	**Adj. R^2***
Brucite [100]	11.12 ± 0.51	0.41 ± 0.03	-1.68 ± 0.15	4.37 ± 0.48	0.92
Brucite [001]	1.03 ± 0.12	0.33 ± 0.05	-0.88 ± 0.08	1.01 ± 0.13	0.93
Periclase[100]#	53.82 ± 1.79	1.34 ± 0.11	2.46 ± 0.28	-2.86 ± 0.54	0.98

*Adjusted coefficient of determination (R^2) for the third-order polynomial fit.

#Experimental data for periclase (MgO) up to 60 GPa at room temperature was taken from Dalton et al. (2013).

Figure 1.

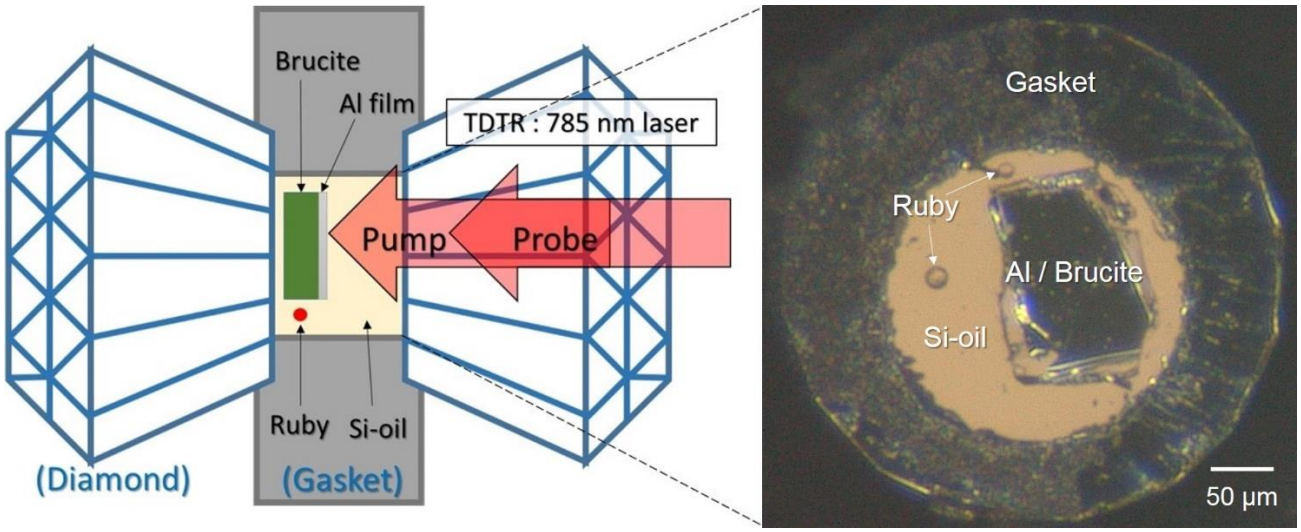

Figure 2.

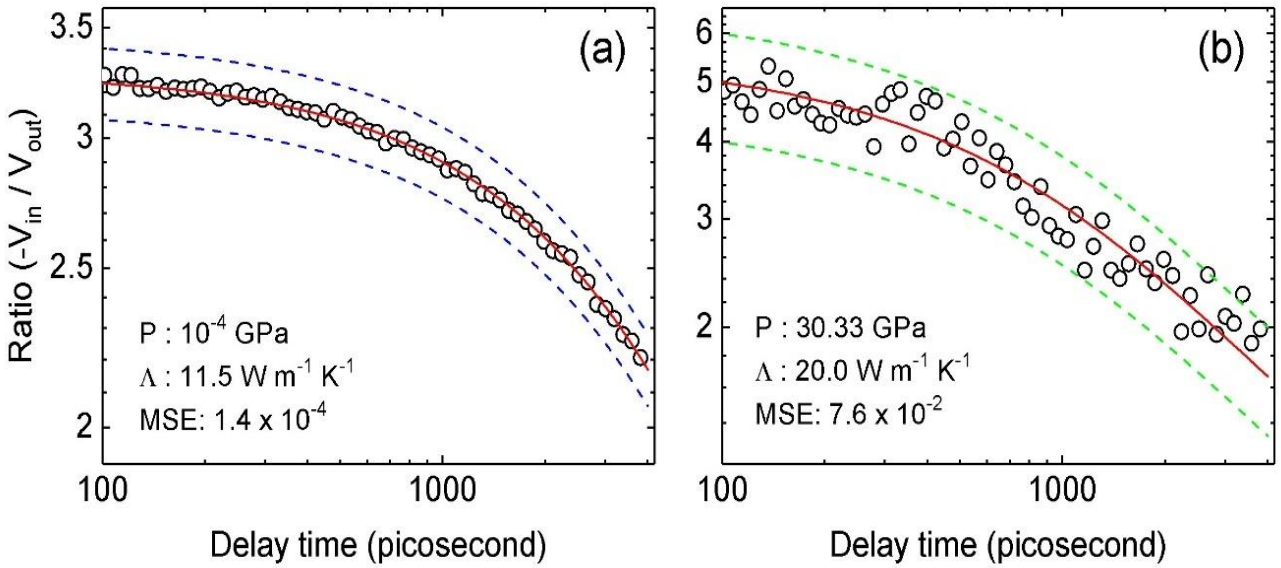

578 **Figure 3.**

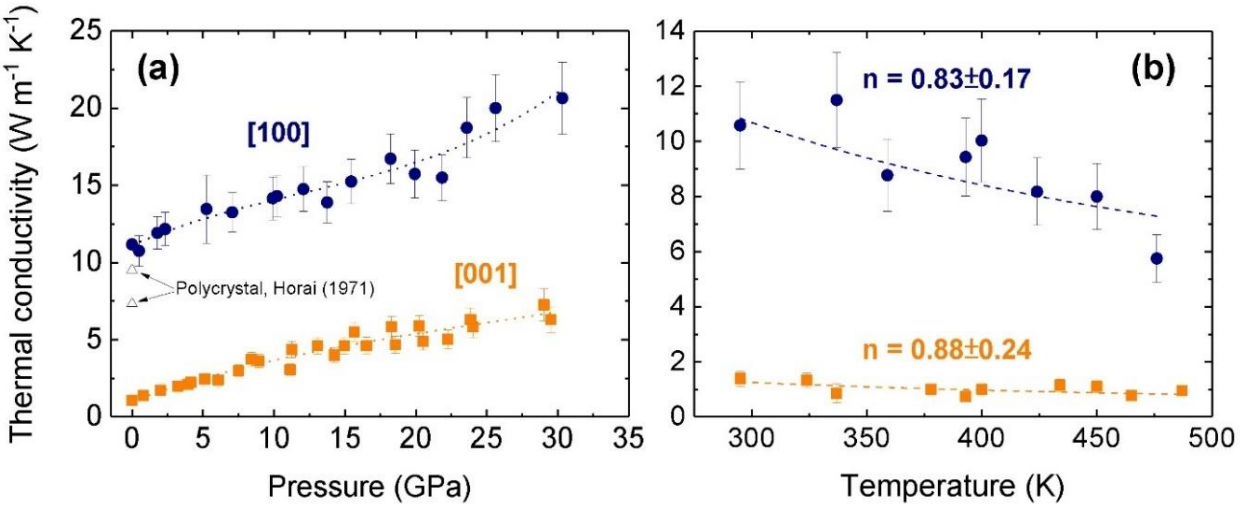

579

580

581 **Figure 4.**

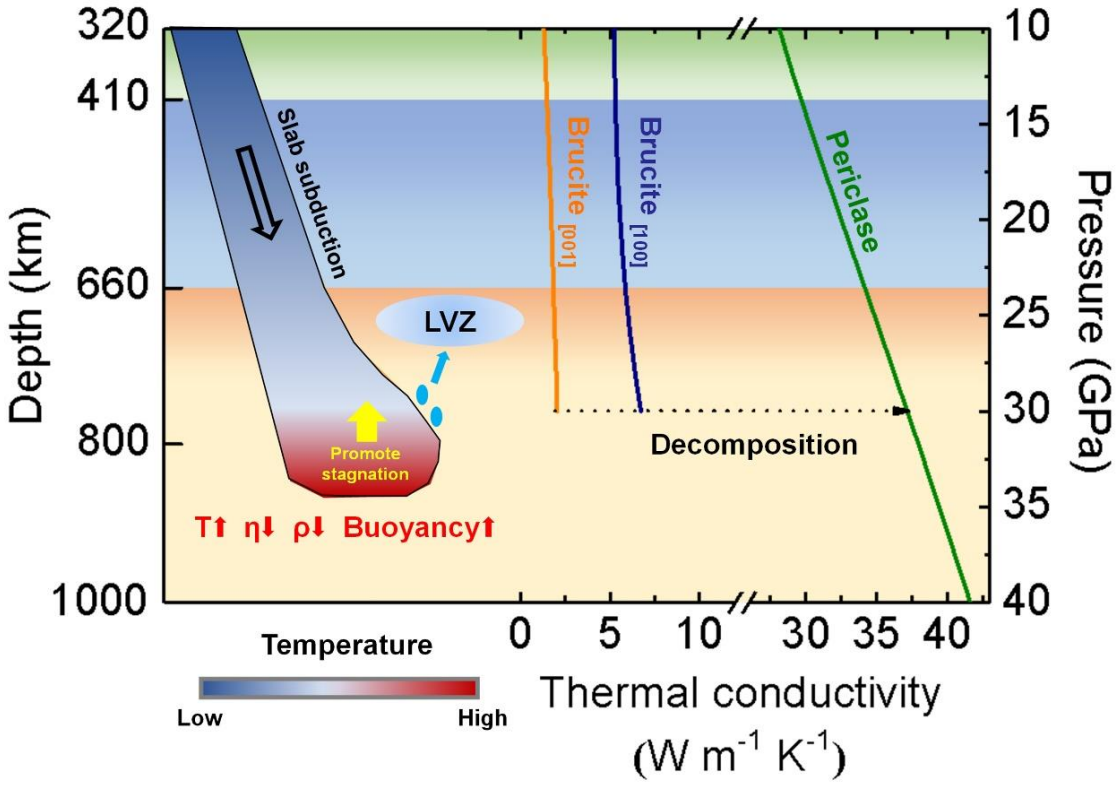

582